

Testing coalescence and statistical-thermal production scenarios for (anti-)(hyper-)nuclei and exotic QCD objects at LHC energies

F. Bellini and A. Kalweit ¹
CERN, EP Department, Geneva (Switzerland)

16th July 2018

(Anti-)(hyper-)nuclei are unique probes of the medium created in proton-proton, proton-Pb, and Pb-Pb collisions at the energies available at the Large Hadron Collider (LHC). Their production is typically discussed within the framework of coalescence and thermal-statistical production models. While it is often argued that these two approaches are not distinguishable, we present a detailed study of both theories which reveals large differences between the two scenarios for the production of objects with extended wave-functions. Both models give similar predictions and show similar agreement with experimental data for (anti-)deuterons and (anti-)³He nuclei, but they largely differ in their description of (anti-)hyper-triton production. The thermal-statistical model is found to be in agreement with results in central Pb-Pb collisions even though fragile objects such as light (anti-)(hyper-)nuclei should be destroyed in hadronic interactions after the chemical freeze-out of the system. Our findings highlight the unique potential of ultra-relativistic heavy-ion collisions as a laboratory to clarify the internal structure of exotic QCD objects and can serve as a basis for more refined calculations in the future.

¹Contacts: fbellini@cern.ch, akalweit@cern.ch

1. Introduction

The formation of light anti- and hyper-nuclei in high energy proton-proton (pp), proton-nucleus (pA) and nucleus-nucleus (AA) collisions provides unique observables for the study of the system created in these collisions. In addition, these studies might shed light on the internal structure of the formed objects themselves. In this context, nuclei and hyper-nuclei are special objects with respect to non-composite hadrons (such as pions, protons, kaons, etc.), because their size (i.e. the extension of their wave-function) is comparable to a fraction or the whole system created in the collision [1]. The relevant known properties of the objects under study here are summarised in Table 1. As quantum-mechanical objects, their size is typically defined as the rms of their (charge) wave function, which corresponds to about 2 fm for light (anti-)nuclei as obtained from electron scattering experiments. Not much is known experimentally about the wave-functions of hyper-nuclei and other exotic QCD objects. For the hyper-triton, theoretical calculations indicate a rms of the wave-function of about 5 fm [2], which is significantly larger than that of non-strange $A = 3$ nuclei. This is driven by the average separation of the Λ with respect to the two other nucleons which is expected to amount to up to 10 fm [2]. Halo nuclei as ${}^6\text{He}$ would therefore be an ideal complement to this study, but they remain out of the experimental reach in high-energy experiments in the near future.

Since about sixty years, coalescence models have been used to describe the formation of composite objects (see for instance [3–11] and references therein). Surprisingly, thermal-statistical models have been successful in describing not only light-flavour particle production, but also that of light (anti-)(hyper-)nuclei across a wide range of energies in nucleus-nucleus collisions [12, 13]. In this approach, particles are produced from a fireball in thermal and kinetic equilibrium with temperatures of the order of $T_{chem} \approx 156$ MeV that are near the temperature of the QCD phase transition boundary, as predicted by lattice QCD calculations [14, 15]. Particle abundances are fixed at chemical freeze-out, when inelastic collisions cease. Further elastic and pseudo-elastic collisions occur among the components of the expanding fireball, that can affect the spectral shapes and the measurable yields of short-lived (strongly decaying) hadronic resonances. Once the particle density of the system is so low that the mean free path for elastic collisions is larger than the size of the system, the fireball freezes-out kinetically. At LHC energies, this is seen to occur when the system has reached temperatures of the order of $T_{kin} \approx 90$ MeV [16]. In such a dense and hot environment, composite objects with binding energies that are small with respect to the temperature of the system, appear as “fragile” objects. For instance, the binding energy of the deuteron is $B_{E,d} = 2.2$ MeV $\ll T_{chem}, T_{kin}$. As a matter of fact, the cross-section for pion-induced deuteron breakup is significantly larger than the typical (pseudo)-elastic cross-sections for the re-scattering of hadronic resonance decay products [17–19]. Similarly, the elastic cross-section which drives the deuteron spectra to kinetic equilibration in central heavy-ion collisions [20] is smaller than the breakup cross-section [17–19]. Based on this, the deuterons produced at chemical freeze-out would be expected not to survive the hadronic phase of the medium expansion, yet their production is measured to be consistent to the predictions from statistical-thermal models and they develop also a non-zero elliptic flow which is consistent with a common radial expansion together with the non-composite hadrons [20]. Several solutions have been proposed to solve this “light (anti-)nuclei puzzle”: (a.) a sudden freeze-out at the QGP-hadron phase boundary, (b.) the thermal production of these objects as compact quark bags [12], and (c.) the coincidence of coalescence mechanism with that of thermal production [7, 21]. Data from rescattering of short-lived hadronic resonances indicate that the system undergoes a long-lasting hadronic phase before decoupling [22], thus strongly disfavouring hypothesis (a.). While hypothesis (b.) cannot presently be tested beyond the agreement of measured (anti-)nuclei production yields with statistical-thermal model predictions, hypothesis (c.) is scrutinised in the present work.

To this purpose, we compare to models the existing data from the LHC. For the first time, these data allow for the systematic study of the light (anti-)(hyper-)nuclei production as a function of the system and object size. In the nucleon-coalescence approach, nuclei are formed at

Mass number	Nucleus	Compo- sition	B_E (MeV)	Spin J_A	(Charge) rms radius λ_A^{meas} (fm)	Harmonic oscillator size parameter r_A (fm)	Refs.
A = 2	d	pn	2.224575 (9)	1	2.1413 ± 0.0025	3.2	[23, 24]
A = 3	^3H	pnn	8.4817986 (20)	1/2	1.755 ± 0.086	2.15	[25]
	^3He	ppn	7.7180428 (23)	1/2	1.959 ± 0.030	2.48	[25]
	$^3_\Lambda\text{H}$	p Λ n	0.13 ± 0.05	1/2	$4.9 - 10.0$	$6.8 - 14.1$	[2, 26]
A = 4	^4He	ppnn	28.29566 (20)	0	1.6755 ± 0.0028	1.9	[27, 28]
	$^4_\Lambda\text{H}$	p Λ nn	2.04 ± 0.04	0	$2.0 - 3.8$	$2.4 - 4.9$	[2, 26]
	$^4_{\Lambda\Lambda}\text{H}$	p $\Lambda\Lambda$ n	$0.39 - 0.51$	1	$4.2 - 7.1$	$5.5 - 9.4$	[2]
	$^4_\Lambda\text{He}$	pp Λ n	2.39 ± 0.03	0	$2.0 - 3.8$	$2.4 - 4.9$	[2, 26]

Table 1: Properties of nuclei and hyper-nuclei with mass number $A \leq 4$. B_E is the binding energy in MeV. The size of the nucleus is given in terms of the (charge) rms radius of the wavefunction, λ_A . The size parameter of the wave-function of the harmonic oscillator potential, r_A , is chosen such that the measured/expected rms is approximately reproduced. Details are given in Appendix A. Please note that the proton rms charge radius $\lambda_p = 0.879(8)$ fm [29] is subtracted quadratically from the measured rms charge radius λ_A^{meas} of the nucleus $\lambda_A = \sqrt{(\lambda_A^{meas})^2 - \lambda_p^2}$ to account for the finite extension of the constituents. Implicitly we assume here that $\lambda_\Lambda \approx \lambda_n \approx \lambda_p$. References are given in the last column. The spin of $^4_{\Lambda\Lambda}\text{H}$ is discussed in the text of [2].

kinetic freeze-out by coalescence of nucleons that are nearby in space and have similar velocities. The coalescence model is reviewed in Section 2, starting from its simplest form (uncorrelated nucleon emission from a point-like source) to the full space-time evolution picture as discussed in [7]. In section 3, a blast-wave parameterisation for particle transverse momentum spectra in combination with predictions from the statistical-thermal model for the yields is used as an alternative approach. The direct comparison of the two approaches and the comparison with data are discussed in section 4. We find that a systematic study of the coalescence parameter B_A provides an important discrimination power between the two approaches.

A quantitative direct comparison of the two production scenarios has been proposed recently in [30], that resulted in the proposal to study the production rates of nuclei with similar mass but very different internal structure, in particular of ^4He and ^4Li [10]. However, as the ^4Li is not stable with respect to strong decay, its measurement is experimentally very challenging and probably less constraining than the comparison with hyper-nuclei proposed here. We propose that B_A is systematically measured in all collision systems by exploiting the large statistics sample that will be available with the LHC Run 3 & 4, in order to rule out or support the aforementioned scenarios. As a matter of fact, the upcoming years of LHC data taking provide a unique opportunity for the final understanding of (anti-)(hyper-)nuclei production. Setting a final word on the production mechanisms is not only in the interest of the heavy-ion community, but has a broader application in astrophysics and dark-matter searches, by representing an essential input for the measurement of (anti-)nuclei in space with ongoing [31] and future [32, 33] experiments. In addition to this, the study of light(anti-)nuclei might serve as a baseline for understanding the debated nature of exotic states such as the X(3872), that has been interpreted as tetraquark state or hadronic molecule [8, 34].

2. Coalescence approach

2.1. Simple coalescence

In the coalescence picture, nucleons produced in the collision coalesce into nuclei if they are close in space and have similar velocities [3, 4]. For a nucleus with mass number $A = Z + N$, the coalescence probability is typically quantified in terms of the coalescence parameter B_A , which is defined as

$$E_A \frac{d^3 N_A}{dp_A^3} = B_A \left(E_p \frac{d^3 N_p}{dp_p^3} \right)^Z \bigg|_{\vec{p}_p = \frac{\vec{p}_A}{A}} \left(E_n \frac{d^3 N_n}{dp_n^3} \right)^N \bigg|_{\vec{p}_n = \frac{\vec{p}_A}{A}}, \quad (1)$$

where $p_{p,n}$ are the momenta of the proton and neutron and $E_{p,n}$ their energies. Since in the LHC collision energy regime the number of produced protons and neutrons at midrapidity is expected to be equal, the equation simplifies to

$$E_A \frac{d^3 N_A}{dp_A^3} = B_A \left(E_p \frac{d^3 N_p}{dp_p^3} \right)^A \bigg|_{\vec{p}_p = \frac{\vec{p}_A}{A}}. \quad (2)$$

Moreover, the LHC is particularly suited for the production of anti-nuclei, since the number of baryons and anti-baryons is essentially equal at midrapidity [35]. As a consequence, also the anti-particle to particle ratio for the light (hyper-)nuclei considered in this work is measured to be consistent with unity in pp, p-Pb and Pb-Pb collisions [20, 36–38]. In a simple coalescence approach, the coalescence parameter is expected to be independent of p_T and of the object size with respect to the volume of particle emission (hereafter referred to as “source volume” or “source size”). In this naive expectation, the number of nuclei produced by coalescence increases with increasing number of nucleons produced in the collision. If the nucleon number increases with the event multiplicity, so does the number of (anti-)nuclei. While this picture is found to be approximately valid in pp and p-Pb collisions [36, 37], it breaks down in Pb-Pb collisions, that exhibit a strong decrease of B_A with the centrality of the collision [39]. In addition, the elliptic flow of deuterons cannot be explained by simple coalescence [20].

2.2. Advanced coalescence

In contrast to the simple approach described in the previous section, a more advanced coalescence model takes into account the size of the particle emission source, as the coalescence probability naturally decreases for two nucleons with similar momenta that are produced far apart in configuration space. While there are several approaches to address this effect [5, 6], in our study we rely on the formalism proposed in [7]. The authors use a density matrix approach to calculate the coalescence probability and the invariant momentum spectra of deuterons and anti-deuterons in heavy-ion collisions. They consider the coalescence of nucleons within a source that is rapidly expanding under collective flow. The fact that the coalescence probability is anti-proportional to the source volume can already be understood in the classical phase-space picture as due simply to the separation in configuration space. Because coalescence is a quantum-mechanical process, however, the classical definition of phase space does not apply and it is replaced by the Wigner formalism. Therefore, most coalescence models, including [7], determine the production probability of a nucleon cluster as by the overlap of the Wigner function of its internal wave-function with the phase-space distributions of the constituent particles.

The wave-functions of the objects under study are approximated by the ground-state wave-functions of an isotropic spherical harmonic oscillator as in [7] with a characteristic size parameter r_A . For the deuteron ($A = 2$) wave-function $\varphi_d(\vec{r})$, one obtains

$$\varphi_d(\vec{r}) = (\pi r_d^2)^{-3/4} \exp \left(-\frac{r^2}{2r_d^2} \right). \quad (3)$$

For nuclei with $A > 2$, analogous forms exist (see Appendix A and B for details). The relation between the characteristic size parameter r_A and the rms of the wave-function was derived in [40] as

$$\lambda_A^2 = \frac{3}{2} \frac{A-1}{A} \frac{r_A^2}{2} \quad (4)$$

for point-like constituents. In particular, we obtain $r_d = \sqrt{8/3}\lambda_2$ for $A = 2$, $r_3 = \sqrt{2}\lambda_3$ for $A = 3$, and $r_4 = \sqrt{16/9}\lambda_4$ for $A = 4$ (see Appendix A and B for details).

This ansatz allows to derive in the following a set of analytic formulas which can be used for the calculation of coalescence predictions. In Tab. 1, we therefore do not list only the rms of the wavefunction, but also the size parameter of the harmonic oscillator function, r_A , derived according to these relations. The approximation of the wave-function with a gaussian form can be further refined with these more realistic parameterisations, e.g. the Hulthen parameterisation for the deuteron [6] or a Λ -deuteron parameterisation for the hyper-triton as done for central collisions in [41]. We encourage future more rigorous numerical studies that address the calculation of coalescence probabilities with these more realistic wave-functions. Nonetheless, in this work, we decide to follow the gaussian ansatz in order to obtain more intuitive and fully analytic solutions that highlight the sensitivity to the size of the source (i.e. the centrality dependence) and that of the (hyper-)nucleus. In particular, the gaussian assumption allows one to describe the extension of the wave-function with one single parameter r_A .

The quantum mechanical nature of the coalescence products is explicitly accounted for by means of an average quantum mechanical correction factor, $\langle C_A \rangle$. In the case of the deuteron, the quantum mechanical correction factor $\langle C_d \rangle$ has been approximated as

$$\langle C_d \rangle \approx \frac{1}{\left[1 + \left(\frac{r_d}{2R_\perp(m_T)}\right)^2\right] \sqrt{1 + \left(\frac{r_d}{2R_\parallel(m_T)}\right)^2}} \quad (5)$$

where r_d is the radius of the deuteron, R_\perp and R_\parallel are the lengths of homogeneity of the coalescence volume and m_T is the transverse mass of the coalescing nucleons. The size of the nucleus enters in the determination of the coalescence parameter B_2 via the quantum-mechanical correction factor $\langle C_d \rangle$, as well as the homogeneity volume $R_\perp^2 R_\parallel$, according to the relation

$$B_2 = \frac{3\pi^{3/2}\langle C_d \rangle}{2m_T R_\perp^2(m_T) R_\parallel(m_T)} \quad (6)$$

which is the main result of [7]. It is interesting to note that the coalescence parameter decreases with increasing volume, as expected. In addition to this, the quantum mechanical correction factor introduces a length scale defined by the deuteron size relative to the source size in the calculation of B_2 , which reflects the coalescence probability. If we assume that $R_\perp \approx R_\parallel \approx R$, Eqs. 5 and 6 simplify to

$$\langle C_d \rangle \approx \left[1 + \left(\frac{r_d}{2R(m_T)}\right)^2\right]^{-3/2} \quad (7)$$

and

$$B_2 = \frac{3\pi^{3/2}\langle C_d \rangle}{2m_T R^3(m_T)}. \quad (8)$$

Figure 1 shows the source radius (R) dependence of the quantum-mechanical correction factor (on the left) and the coalescence parameter B_2 (on the right), calculated assuming (a.) a point-like nucleus $r_d = 0$, (b.) $r_d = 0.3$ fm, (c.) the actual value which reproduces the measured rms radius of the deuteron $r_d = 3.2$ fm [24], (d.) a larger, unrealistic value of $r_d = 10$ fm. As can be seen in Fig. 1, the quantum-mechanical correction factor leads to a significant suppression in the production of those objects whose radius is large compared to that of the source.

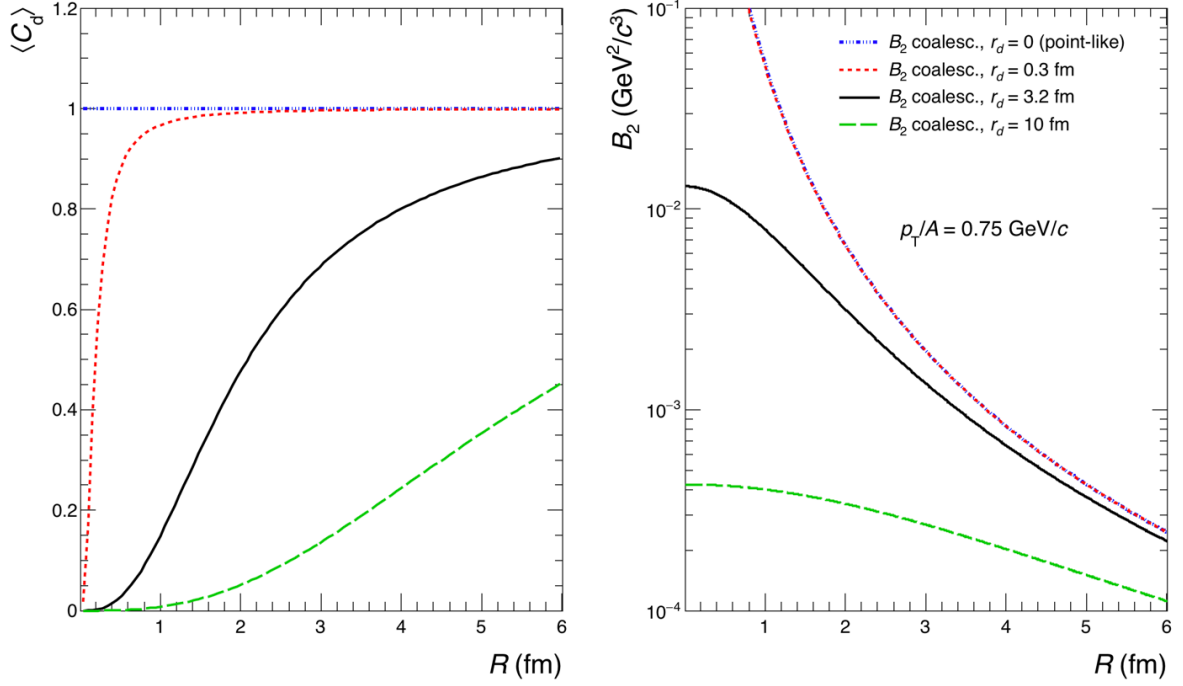


Figure 1: The quantum mechanical correction factor $\langle C_d \rangle$ (left panel, see Eq. 7) and the coalescence parameter B_2 for deuteron (right panel, see Eq. 8) as a function of the radius of the source, R , calculated assuming a size parameter for the deuteron $r_d = 0, 0.3, 3.2$ and 10 fm.

Following the approach and discussion presented in [9], Eq. 5 may be generalised as

$$\langle C_A \rangle = \prod_{i=1,2,3} \left(1 + \frac{r^2}{4R_i^2} \right)^{-\frac{1}{2}(A-1)} \quad (9)$$

for mass number A and the radii R_i that describe the volume of the emitting source. Similarly, the coalescence parameter B_A for a nucleus with mass number A and spin J_A is generalised in [7] as

$$B_A = \frac{2J_A + 1}{2^A} \frac{1}{\sqrt{A}} \langle C_A \rangle \left(\frac{(2\pi)^{3/2}}{m_T \prod_{i=1,2,3} R_i} \right)^{A-1}. \quad (10)$$

In particular, for the case of ${}^3\text{He}$ with $A = 3$ and $J = 1/2$, Eq. 10 becomes the Eq. 9 presented in [9]:

$$B_3 = \frac{(2\pi)^3}{4\sqrt{3}} \langle C_3 \rangle (m_T \prod_{i=1,2,3} R_i)^{-2} \quad (11)$$

where

$$\langle C_3 \rangle \approx \prod_{i=1,2,3} \left(1 + \frac{r_3^2}{4R_i^2} \right)^{-1}. \quad (12)$$

In summary, under the assumption $R_1 \approx R_2 \approx R_3 \approx R$ as in [9] (see details in next section) and by combining Eq. 10 and Eq. 9, we obtain the following general expression for the coalescence parameter:

$$B_A = \frac{2J_A + 1}{2^A} \frac{1}{\sqrt{A}} \frac{1}{m_T^{A-1}} \left(\frac{2\pi}{R^2 + (\frac{r_A}{2})^2} \right)^{3/2(A-1)}. \quad (13)$$

This formula can be used to compare the predicted B_A with experimental data directly.

We understand the relation between B_A and the radii as follows: for small radii of the source, as $R \rightarrow 0$, the coalescence probability appears to be anti-proportional to the harmonic oscillator size parameter r_A , and thus proportional to the depth of the attractive potential in the harmonic oscillator picture (and thus to the nucleus binding energy). Quite naturally, the allowed momentum difference between the coalescing nucleons is larger for more attractive, i.e. deeper, potentials. For large source volume, i.e. $R \gg r_A$, the coalescence probability is dominated by the classical phase-space separation, and thus decreases for large differences in configuration space.

2.3. Source volume

We identify the source volume as the effective sub-volume of the whole system that is governed by the homogeneity length of the interacting nucleons, as in [7]. In addition, the same authors claim that this volume is experimentally accessible with Hanbury-Brown-Twiss (HBT) interferometry. The experimental results are typically obtained following the Bertsch-Pratt (BP) parameterisation ($R_{out}, R_{side}, R_{long}$), while the coalescence model described in Section 2 expresses the volume in terms of the Yano-Koonin-Podgoretskii (YKP) parameterisation. As discussed in Appendix C, we identify $R_{\perp} = R_{side}$ and $R_{\parallel} = R_{long}$. We then take $R = (R_{\perp}^2 R_{\parallel})^{1/3} \approx (R_{side}^2 R_{long})^{1/3}$.

Experimentally, the size of the effective volume can be controlled by selecting different collision geometries, i.e. different centrality classes [42]. In heavy-ion collisions the HBT radii are known to scale with the cubic root of the average charged particle multiplicity density $\langle dN_{ch}/d\eta \rangle^{1/3}$ [1], and to depend on the pair average transverse momentum $\langle k_T \rangle$ [43]. In the following, we make the simplifying assumption that the scaling with $\langle dN_{ch}/d\eta \rangle^{1/3}$ holds across collision systems, which is approximately fulfilled in data [44]. In contrast to [9], we therefore do not explicitly use the measured HBT radii in our study, but we derive the radii from the measured $\langle dN_{ch}/d\eta \rangle$ according to the following relation:

$$R = a \langle dN_{ch}/d\eta \rangle^{1/3} + b \quad (14)$$

The coefficients, $a = 0.339$ and $b = 0.128$ (in units of fm), have been determined by fitting linearly the ALICE data, and the parameterisation is reported in Fig. 2. The values we obtain by interpolating the geometric mean of the measured radii are consistent with the radii from kaon femtoscopy for $m_T \approx 1$ GeV/c in low-multiplicity pp collisions [45] and the radii from pion femtoscopy in high-multiplicity Pb-Pb collisions at the highest available $k_T \approx 0.9$ GeV/c [1]. The highest k_T bin was chosen as it is closest in m_T to the lowest transverse momentum per nucleon ($p_T/A \approx 0.8$ GeV/c) accessible by ALICE for the measurement of nuclei production. Ideally, one would use the proton femtosopic radii for such a study, but given that these measurements are not available in all collision systems and centralities, we assume that m_T -scaling holds for HBT radii [46].

3. Statistical-thermal approach and blast-wave

In the statistical-thermal approach, the yields (dN/dy) of light anti- and hyper-nuclei are very sensitive to the chemical freeze-out temperature T_{chem} due to their large mass m and approximately scale as $dN/dy \propto \exp(-m/T_{chem})$. As a matter of fact, the chemical freeze-out temperature defines the only scale in this model, since at the LHC the chemical potentials which ensure the conservation of baryon number (μ_B), strangeness (μ_S), and electric charge (μ_Q) are negligible. In contrast to the coalescence approach, the current implementations [47–49] of the

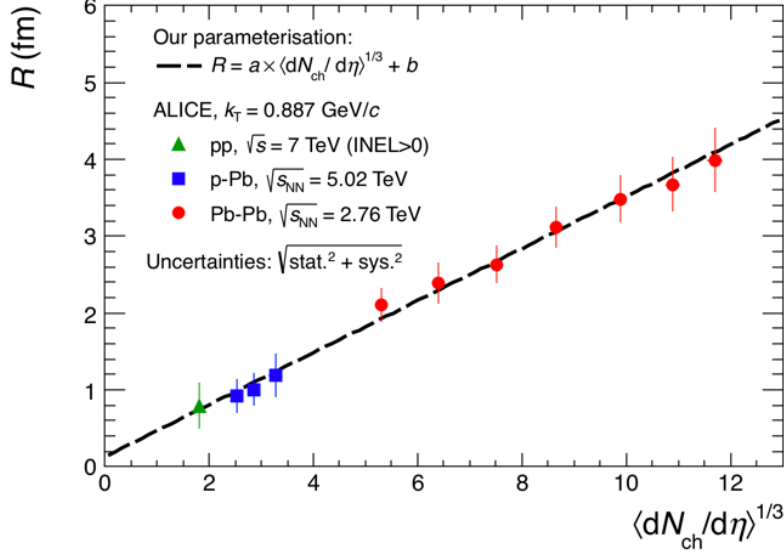


Figure 2: Parameterisation of the dependence of the source radius on multiplicity assumed in this paper, compared to HBT data from [1, 44, 45]. The radius R and the parameters a and b are in units of fm.

221 statistical-thermal model provide only p_T -integrated yields and not the p_T -differential hadron
 222 spectra. In order to fill this gap, and for the purposes of this exercise, p_T spectra have been
 223 modelled using a blast-wave [50] parameterization. When extracting the predicted spectrum for
 224 a given particle species (proton, Λ , deuteron, ^3He), the parameters of the blast-wave (average
 225 radial flow velocity $\langle\beta_T\rangle$, kinetic freeze-out temperature T_{kin} , and velocity profile n) are fixed
 226 to the values obtained from the simultaneous fit to the pion, kaon and proton spectra measured
 227 in Pb–Pb collisions as a function of centrality by ALICE [16]. The normalisation is fixed using
 228 the p_T -integrated deuteron-to-pion ratio and ^3He -to-pion ratio predicted by the GSI-Heidelberg
 229 model with $T_{chem} = 156$ MeV, multiplied by the pion yield measured by ALICE [16]. This
 230 choice, as opposed to using ratio to proton, is motivated by the fact that the measured proton
 231 yield is seen to be slightly underestimated by the thermal model predictions at the LHC [51].
 232 In the case of hyper-triton, a slightly different procedure is chosen, namely the normalisation
 233 for $^3_\Lambda\text{H}$ is extracted from the statistical-thermal model prediction of the strangeness population
 234 factor S_3 multiplied by the measured Λ/p ratio [16, 52] and the measured ^3He yield [39]. Based
 235 on the spectra obtained in this way, we calculate the corresponding coalescence parameters for
 236 a given p_T/A and compare it with coalescence expectations. Because we use experimental data
 237 to constrain the blast-wave prediction as well as the normalisation, and because such data are
 238 provided for given centrality classes, we use the corresponding $\langle dN_{ch}/d\eta \rangle$ in each class to esti-
 239 mate the system radius based on the parameterisation discussed in Sec. 2.3. In contrast to the
 240 coalescence approach, which explicitly depends on the size of the produced object with respect to
 241 the system size, the object size does not enter in the formulation of the blast-wave model. Being
 242 a simplified hydrodynamic model, the latter treats the system as a continuum and is not particle
 243 based. The thermal model on the other hand, implements eigenvolume corrections by fixing the
 244 object radius as an external parameter (0.3 fm in the case of baryons for the GSI-Heidelberg
 245 model used here). We refer to the literature for the extensive discussions on the validity of the
 246 eigenvolume correction for light anti- and hyper-nuclei [53] and the relation with the possible
 247 production of these objects as compact quark bags [12].

4. Comparison with experimental data

4.1. Constraining the source volume with data

Data on anti- and hyper-nuclei production at LHC energies and different collision systems have been released by the ALICE Collaboration in recent years [20, 36, 38, 39]. In Fig. 3 we compare the coalescence parameter for deuteron (B_2) from the coalescence model (see Eqs. 6 and 8, with $r_d = 3.2$ fm) to the ALICE data for Pb-Pb collisions at $\sqrt{s_{NN}} = 2.76$ TeV and pp collisions at $\sqrt{s} = 7$ TeV. For pp collisions, data in [36] are given for inelastic (INEL) collisions. In order to facilitate the comparison with future multiplicity-dependent data given in the INEL>0 class, we have rescaled the B_2 and B_3 by the ratio of the charged particle multiplicity density in these two event classes [54]. First, the parameterisation of the system radius fitted to the HBT data as described in Sec. 2.3 (labeled in the following as "parameterisation A") is used to map the $\langle dN_{ch}/d\eta \rangle$ to the source size (top left panel of Fig. 3). We notice already at this point that the coalescence volume from parameterisation A radii leads to discrepancies with respect to the curve from the coalescence calculation, and in particular, we notice that the model would require a larger radius for a given value of B_2 for Pb-Pb collisions.

In a second step the radius is tuned such that the data points for (anti-)deuterons fall onto the coalescence prediction (top right panel of Fig. 3). We find that the parameters of Eq. 14 turn out to be $a = 0.473$ and $b = 0$. With this second parameterisation (labeled as "B" in the following), we investigate the agreement of the model with the measured coalescence parameter for ${}^3\text{He}$, B_3 . As shown in the lower panels of Fig. 3, also in the case of B_3 , a tension between the model and the data is found for parameterisation A, which ameliorates for the parameterisation B, tuned to the (anti-)deuteron data. The strength of this approach is given by the fact that the coalescence volume is constrained with the more differential (anti-)deuteron data assuming that the latter is the same for all anti- and hyper-nuclei. It is also noteworthy that any change of the radii parameterisation would result in a shift along the x axis of both B_2 and B_3 data points in the same way, while the theoretical coalescence curve would not be affected.

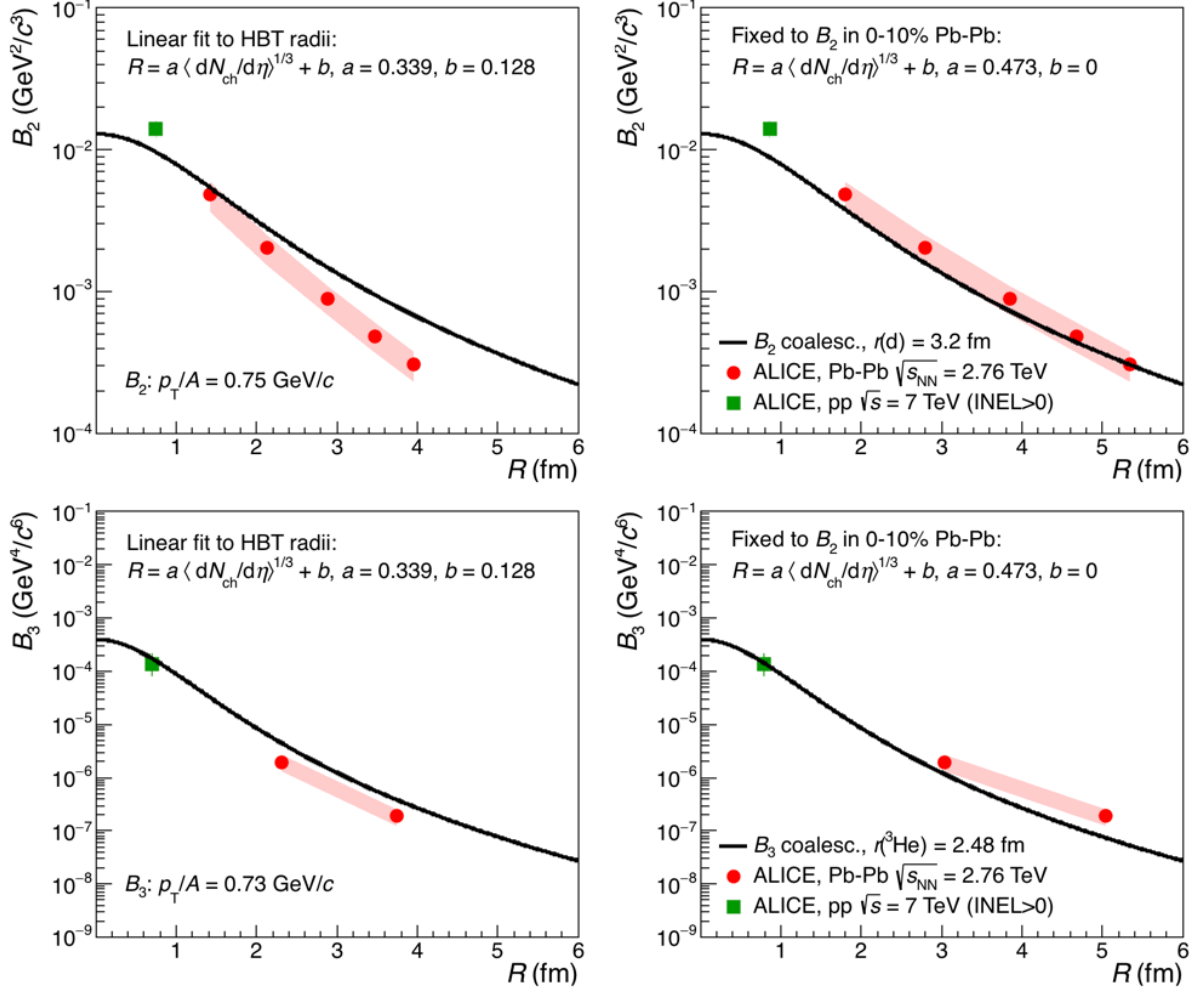


Figure 3: Comparison of the ALICE data from [36, 39] with the coalescence prediction for two different mappings of the $\langle dN_{\text{ch}}/d\eta \rangle$ to the system size R : (left panels) the parameterisation A, fitted to the HBT radii, (right panels) the parameterisation B, tuned to the B_2 values in central Pb-Pb collisions. The radius R and the parameters a and b are in units of fm.

4.2. Thermal and coalescence model for $A = 2, 3$ anti- and hyper-nuclei

In Fig. 4, the available data for (anti-)deuterons, (anti-) ^3He and $^3_\Lambda\text{H}$ [38] are compared to both coalescence and thermal model predictions. For the coalescence predictions, the radius parameterisation B is used, as discussed in Sec. 4.1. The combined thermal model and blast-wave predictions are calculated as described in Sec. 3.

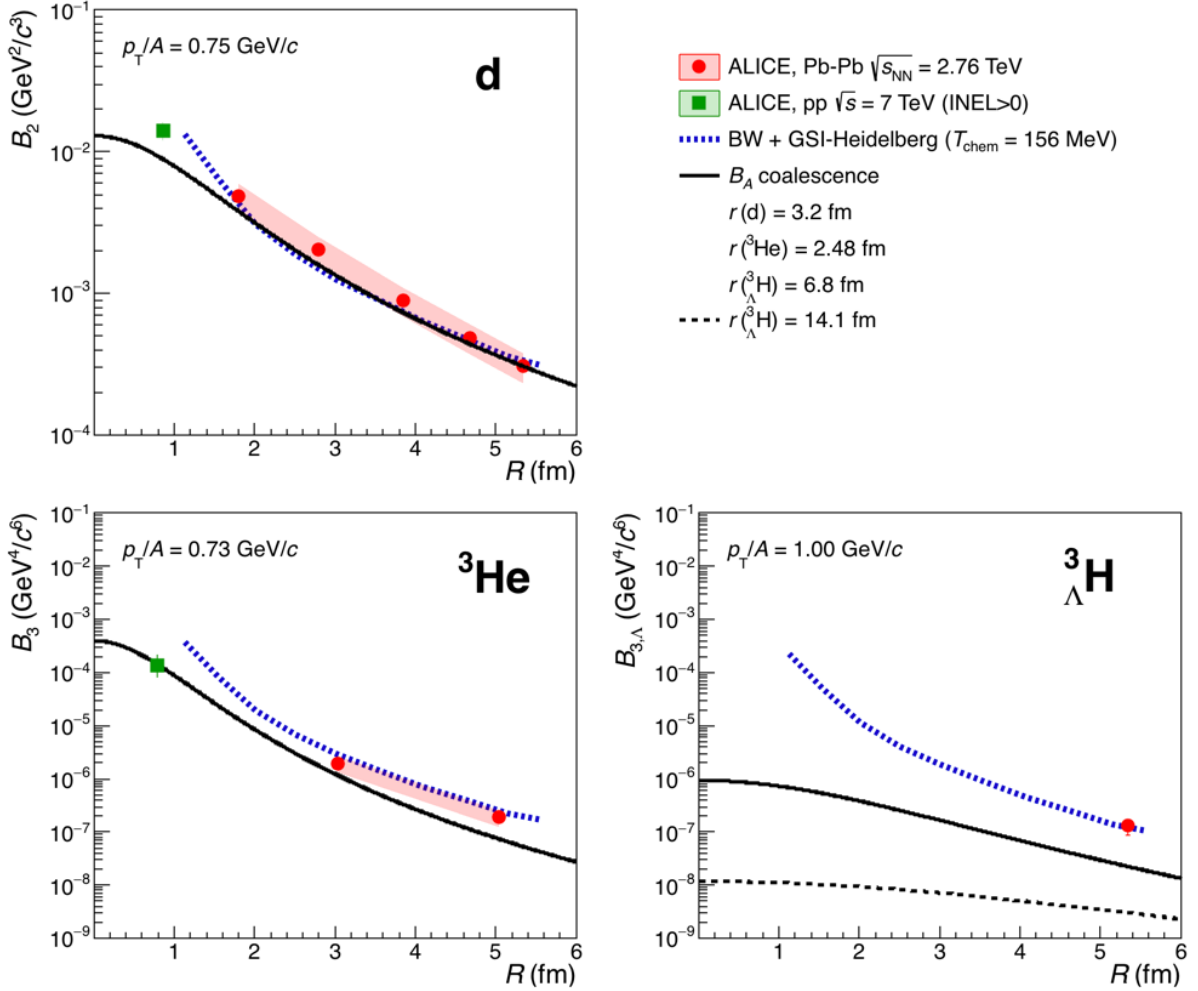


Figure 4: Comparison of the coalescence parameters measured by ALICE (solid markers) for deuterons (upper left panel), ^3He (lower left panel) and $^3_\Lambda\text{H}$ (lower right panel) in pp [36] and Pb–Pb [38, 39] collisions with the thermal+BW model expectations (dotted line) and the coalescence predictions (solid lines). Parameterisation B has been used to map the charged particle multiplicity density into the radius R of the source (see text for details). The dashed line in the lower right panel corresponds to the coalescence prediction for the $^3_\Lambda\text{H}$ with a larger radius.

As a first observation, one sees that for deuterons both approaches lead to similar predictions and give a reasonable description of the experimental data for $R \gtrsim 1.6$ fm. For ^3He the two models exhibit a qualitatively similar trend as a function of R , but they differ by a factor of about 2. The limited amount of data that is currently available is consistent with both models within 2σ to 3σ , where σ is the total uncertainty on the data. Both approaches show large differences (a factor 5 to 6 for central Pb–Pb collisions and a factor of about 30 for small radii, $R < 2$ fm) for the $^3_\Lambda\text{H}$ caused by the significantly larger size of $^3_\Lambda\text{H}$ with respect to ^3He . As a matter of fact, the only datapoint available so far in Pb–Pb collisions is in agreement with the

thermal+BW model but not with coalescence. The difference between data and the coalescence model is about 6σ . However, it is to be kept in mind that the considerations expressed here are subject to the validity of our assumptions, *in primis* the usage of a gaussian form for the wave-function. Some authors argue that the difference of data to the coalescence model might be explained by a later formation through the coalescence of Λ s and deuterons [41]. In addition, the presence of an excited state with $J = 3/2$ of the hyper-triton would significantly enhance the phase space for its production. This is not considered here as there is no evidence for the existence of such an excited state [55]. According to our understanding, in both the coalescence and the thermal model calculations the presence of excited states enters via a spin degeneracy factor $(2J_A + 1)$ and thus the predictions would increase by the same factor.

Most importantly, Fig. 4 shows that the difference between the two approaches increases with decreasing source volume, thus underlining the need for additional and more precise data as a function of multiplicity or centrality in order to distinguish between the two production scenarios. In the case of ${}^3_\Lambda\text{H}$ we have considered also a prediction from coalescence for a wider wave-function (dashed line in bottom right panel of Fig. 4), which results in even lower production probabilities. This behaviour highlights the unique potential to constrain the wave-function of the particle under study at the moment of its production via precise measurements of the coalescence parameter as a function of the source volume. The curves presented here also explicitly allow for an estimate of the expected hyper-triton production in pp collisions. As it can be seen, the latter is expected to be suppressed by about two orders of magnitude with respect to the production of ${}^3\text{He}$, thus making this measurement a prime candidate for future experimental studies.

5. Summary, conclusions, and outlook

While it is often argued that the coalescence and the thermal model approach give very similar predictions for the production of light anti- and hyper-nuclei in heavy-ion collisions, the study presented here shows that large differences can be expected for hyper-nuclei with extended wave-functions. In the following, we summarise our main conclusions:

1. For the production of $A = 2$ and $A = 3$ (anti-)nuclei in heavy-ion collisions, the thermal and coalescence models give similar predictions for a source volume that is constrained by experimental data on (anti-)deuteron production in central Pb–Pb collisions at the LHC.
2. For the production of hyper-triton, the thermal and coalescence models give very different predictions as a function of source volume. In particular, the yield of hyper-tritons appears to be suppressed by about two orders of magnitude in pp collisions with respect to the production of ${}^3\text{He}$. The very limited amount of data currently available favours the thermal model prediction within our assumptions.
3. Systematic measurements in pp, p–Pb, and Pb–Pb collisions at LHC energies have a unique potential to clarify the production mechanism and the nature of composite QCD objects.

We would like to remark that our study is deliberately based on many simplified assumptions in order to allow for a completely analytical treatment of the problem. Future studies should be based on more realistic approximations, which requires numerical calculations. Moreover, as the study presented here has been carried out for a specific value of transverse momentum per nucleon, it will be interesting to explore further the p_T dependence of the observations made here in comparison to future and currently available data.

In a follow-up publication, we plan to extend our study to predictions for the $A = 4$ systems introduced in Tab. 1 and to more exotic QCD objects like the $X(3872)$. In fact, if the $X(3872)$ corresponds to a loosely bound $\bar{D}^{*0}D^0$ molecule, the rms of its wave-function can be as large as $4.9^{+13.4}_{-1.4}$ fm [56], which is very similar to that of the hyper-triton. Thus, its possible production via a coalescence mechanism in pp collisions would be subject to a similar suppression as the

hyper-triton. Additional theoretical studies and numerical predictions are encouraged in view of the high-luminosity phase of the LHC (Run 3 & 4), where $A = 4$ hyper-nuclei and other rare composite objects might become experimentally accessible.

Acknowledgements

We would like to thank Kfir Blum for inspiring this work. We thank U. Heinz for the useful discussions and the clarification on the equivalence of the Bertsch-Pratt and Yano-Koonin-Podgoretskii parameterisations of the HBT radii. We further acknowledge discussions with Benjamin Doenig, in particular about the production of ${}^3_\Lambda\text{H}$ in pp collisions, and with Eulogio Serradilla Rodriguez. In addition, we would like to thank Juergen Schukraft, Peter Braun-Munzinger, Maximiliano Puccio, Roman Lietava, Natasha Sharma and the colleagues from the ALICE Collaboration for their valuable input.

A. Relation to the Sato-Yazaki coalescence model

The approach of Sato and Yazaki [5] is based on a density matrix model and includes explicitly the system size dependence and wave-function dependence of the coalescence process albeit it assumes a sudden approximation when particles cease their interactions (sudden freeze-out) and thus neglects the collective expansion of the medium in contrast to [7]. It assumes no correlation between different nucleons and no correlation between coordinates in space and momentum. In a heavy ion collisions, such correlations are consequence of hydrodynamical flow. The coalescence process to form a nucleus with mass number $A = Z + N$ is formulated in terms of the momentum per nucleon (p) as

$$\frac{\gamma_A}{\sigma_{A,0}} \frac{d^3\sigma_A}{d^3p} = \left(\frac{4}{3}\pi p_0^3\right)^{A-1} \frac{1}{Z!N!} \left(\frac{\gamma_p}{\sigma_{p,0}} \frac{d^3\sigma_p}{d^3p_p}\right)^Z \left(\frac{\gamma_n}{\sigma_{n,0}} \frac{d^3\sigma_n}{d^3p_n}\right)^N \quad (15)$$

where p_0 corresponds to the coalescence momentum, γ_A and $\gamma_{p,n}$ are the Lorentz factors for the nucleus and the nucleons, respectively. The reaction cross sections are denoted as $\sigma_{i,0}$, where $A = p, n, A$. Assuming that the proton and neutron emission probabilities are equal and that $p_p \approx p_n \equiv p$, this expression relates to the B_A as defined by our Lorentz invariant Eq.(2) as

$$B_A = \left(\frac{4}{3}\pi p_0^3\right)^{A-1} \frac{M}{m^A} \frac{1}{A^3} \frac{1}{Z!N!} \quad (16)$$

where the factor $\frac{1}{A^3}$ results from the transformation of $p_A \rightarrow Ap_{p,n}$ and M corresponds to the nucleus mass and m to the nucleon mass. This expression can be further simplified via the approximation $M \approx Am$ to

$$B_A = \left(\frac{4}{3}\pi p_0^3\right)^{A-1} \frac{1}{m^{A-1}} \frac{1}{A^2} \frac{1}{Z!N!} . \quad (17)$$

For nuclei up to $A = 4$ and the non-relativistic case, Sato and Yazaki derive the following relations for the coalescence momentum p_0 ,

$$A = 2 \quad \frac{4}{3}\pi p_0^3 = \frac{3}{4} 2^{3/2} (4\pi)^{3/2} \left(\frac{\nu_2 \nu}{\nu_2 + \nu}\right)^{3/2} \quad (18)$$

$$A = 3 \quad \frac{1}{2} \left(\frac{4}{3}\pi p_0^3\right)^2 = \frac{1}{4} 3^{3/2} (4\pi)^3 \left(\frac{\nu_3 \nu}{\nu_3 + \nu}\right)^3 \quad (19)$$

$$A = 4 \quad \frac{1}{4} \left(\frac{4}{3}\pi p_0^3\right)^3 = \frac{1}{16} 4^{3/2} (4\pi)^{9/2} \left(\frac{\nu_4 \nu}{\nu_4 + \nu}\right)^{9/2} \quad (20)$$

361 where the size parameter ν relates to the rms radius R_{rms} of the emission source as $\nu = \sqrt{\frac{3}{2R_{rms}}}$,
 362 and ν_A is the size parameter of the nucleus.
 363 Following the generalisation in [6], we thus propose the following parameterisation for the coa-
 364 lesence parameter

$$B_A = \frac{2J_A + 1}{2^A} A^{3/2} (4\pi)^{\frac{3}{2}(A-1)} \left(\frac{\nu_A \nu}{\nu_A + \nu} \right)^{\frac{3}{2}(A-1)} \frac{1}{m^{A-1}} \frac{1}{A^2} \quad (21)$$

$$= \frac{2J_A + 1}{2^A} \frac{1}{m^{A-1}} \frac{1}{\sqrt{A}} (4\pi)^{\frac{3}{2}(A-1)} \left(\frac{\nu_A \nu}{\nu_A + \nu} \right)^{\frac{3}{2}(A-1)}, \quad (22)$$

365 indicating with J_A the spin of the nucleus. Once again, the ν_A parameter corresponds to the
 366 size parameter of the nucleus wave-function, which is assumed to be gaussian (solution to the
 367 isotropic spherical harmonic oscillator potential) of the form [5, 57]:

$$\phi_A = C \exp\left(-\frac{1}{2}\nu_A \sum_{i=1}^A (\vec{x}_i - \vec{X})^2\right) \quad (23)$$

368 with an appropriate normalisation factor C and the coordinate vector \vec{X} of the centre-of-mass
 369 system.

370 We have also verified that our generalisation of Sato-Yazaki provided by Eq. 22 and the
 371 expression derived from Heinz in Eq. 9 become consistent in the limit $R_{rms} \approx R \rightarrow 0$ (point-like
 372 source) and $p_T \rightarrow 0$ (static source), provided that one identifies $\nu_A = 2/r_A^2$. Incidentally, the
 373 same relation between ν_A and r_A can be derived by a straightforward comparison of the nucleus
 374 wave-functions employed by the same authors [5, 7].

375 The parameter ν_A is typically chosen such that the measured rms charge radius λ_A is repro-
 376 duced. The relation between λ_A and ν_A is obtained by a transformation to the Jacobi variables
 377 and performing the integration (see Appendix B). In particular, one obtains for $A < 5$:

$$A = 2 \quad \nu_2 = \frac{3}{4\lambda_2^2} \quad (24)$$

$$A = 3 \quad \nu_3 = \frac{1}{\lambda_3^2} \quad (25)$$

$$A = 4 \quad \nu_4 = \frac{9}{8\lambda_4^2} . \quad (26)$$

B. RMS of a gaussian wave-function for $A = 4$

In this appendix, we show the calculation of the RMS of a gaussian wave-function with the example of $A = 4$. We start from the wave-function

$$\phi_{A=4} = C_4 \exp\left(-\frac{1}{2}\nu_4 \sum_{i=1}^4 (\vec{x}_i - \vec{X})^2\right). \quad (27)$$

Then we introduce the Jacobi variables which are given by

$$\vec{X} = \frac{1}{4}(\vec{x}_1 + \vec{x}_2 + \vec{x}_3 + \vec{x}_4) \quad (28)$$

$$\vec{r}_1 = \vec{x}_2 - \vec{x}_1 \quad (29)$$

$$\vec{r}_2 = \vec{x}_3 - \frac{1}{2}(\vec{x}_1 + \vec{x}_2) \quad (30)$$

$$\vec{r}_3 = \vec{x}_4 - \frac{1}{3}(\vec{x}_1 + \vec{x}_2 + \vec{x}_3). \quad (31)$$

In this parameterisation we can express the squared distance of each nucleon with respect to the centre-of-mass as

$$\sum_{i=1}^4 (\vec{x}_i - \vec{X})^2 = \frac{1}{4}(2\vec{r}_1 + \frac{8}{3}\vec{r}_2 + 3\vec{r}_3)^2. \quad (32)$$

For the following integral calculations we determine the Jacobian as

$$dRdr_1dr_2dr_3 = \left| \det \frac{\partial(R, r_1, r_2, r_3)}{\partial(x_1, x_2, x_3, x_4)} \right| dx_1 dx_2 dx_3 dx_4 \quad (33)$$

$$= \begin{vmatrix} \frac{\partial R}{\partial x_1} & \frac{\partial r_1}{\partial x_1} & \frac{\partial r_2}{\partial x_1} & \frac{\partial r_3}{\partial x_1} \\ \frac{\partial R}{\partial x_2} & \frac{\partial r_1}{\partial x_2} & \frac{\partial r_2}{\partial x_2} & \frac{\partial r_3}{\partial x_2} \\ \frac{\partial R}{\partial x_3} & \frac{\partial r_1}{\partial x_3} & \frac{\partial r_2}{\partial x_3} & \frac{\partial r_3}{\partial x_3} \\ \frac{\partial R}{\partial x_4} & \frac{\partial r_1}{\partial x_4} & \frac{\partial r_2}{\partial x_4} & \frac{\partial r_3}{\partial x_4} \end{vmatrix} dx_1 dx_2 dx_3 dx_4 \quad (34)$$

$$= \begin{vmatrix} \frac{1}{4} & -1 & -\frac{1}{2} & -\frac{1}{3} \\ \frac{1}{4} & 1 & -\frac{1}{2} & -\frac{1}{3} \\ \frac{1}{4} & 0 & 1 & -\frac{1}{3} \\ \frac{1}{4} & 0 & 0 & 1 \end{vmatrix} dx_1 dx_2 dx_3 dx_4 \quad (35)$$

$$= 1 \cdot dx_1 dx_2 dx_3 dx_4. \quad (36)$$

From the requirement $\int |\phi|^2 d\vec{r}_1 d\vec{r}_2 d\vec{r}_3 = 1$, we thus obtain for the normalisation constant C_4 :

$$\frac{1}{C_4^2} = \int \exp^2\left(-\frac{1}{2}\nu_4\left(\frac{1}{2}r_1^2 + \frac{2}{3}r_2^2 + \frac{3}{4}r_3^2\right)\right) d\vec{r}_1 d\vec{r}_2 d\vec{r}_3 \quad (37)$$

where the integration in spherical coordinates is performed with $d\vec{r}_1 = 4\pi r_1^2 dr_1$, $d\vec{r}_2 = \dots$ which gives

$$\frac{1}{C_4^2} = (4\pi)^3 \underbrace{\int_0^\infty r_1^2 \exp\left(-\frac{1}{2}\nu_4 r_1^2\right) dr_1}_{\frac{\sqrt{\pi}}{4} \frac{1}{(\frac{1}{2}\nu_4)^{3/2}}} \underbrace{\int_0^\infty r_2^2 \exp\left(-\frac{2}{3}\nu_4 r_2^2\right) dr_2}_{\frac{\sqrt{\pi}}{4} \frac{1}{(\frac{2}{3}\nu_4)^{3/2}}} \underbrace{\int_0^\infty r_3^2 \exp\left(-\frac{3}{4}\nu_4 r_3^2\right) dr_3}_{\frac{\sqrt{\pi}}{4} \frac{1}{(\frac{3}{4}\nu_4)^{3/2}}} \quad (38)$$

$$= \left(\frac{\pi}{\nu_A}\right)^{9/2} 4^{3/2} \quad (39)$$

$$\Rightarrow C_4 = \left(\frac{\nu_A^3}{4\pi^3}\right)^{3/4}. \quad (40)$$

387 For the rms, we obtain accordingly:

$$\lambda_4^2 = \frac{1}{4} \langle \phi | \sum_{i=1}^4 (\vec{x}_i - \vec{X})^2 | \phi \rangle \quad (41)$$

$$= \int \frac{1}{4} \sum_{i=1}^4 (\vec{x}_i - \vec{X})^2 |\phi|^2 d\vec{x}_1 d\vec{x}_2 d\vec{x}_3 d\vec{x}_4 \quad (42)$$

$$= \frac{C_4^2}{4} \int \left(\frac{1}{2} r_1^2 + \frac{2}{3} r_2^2 + \frac{3}{4} r_3^2 \right) \exp^2 \left(-\frac{1}{2} \nu_A \left(\frac{1}{2} r_1^2 + \frac{2}{3} r_2^2 + \frac{3}{4} r_3^2 \right) \right) d\vec{r}_1 d\vec{r}_2 d\vec{r}_3 \quad (43)$$

$$= \frac{C_4^2}{4} \underbrace{\left(\frac{1}{2} \int r_1^2 \exp \left(-\frac{1}{2} \nu_A r_1^2 \right) \exp \left(-\frac{2}{3} \nu_A r_2^2 \right) \exp \left(-\frac{3}{4} \nu_A r_3^2 \right) d\vec{r}_1 d\vec{r}_2 d\vec{r}_3 \right)}_{\text{I}} \quad (44)$$

$$+ \underbrace{\frac{2}{3} \int r_2^2 \exp \left(-\frac{1}{2} \nu_A r_1^2 \right) \exp \left(-\frac{2}{3} \nu_A r_2^2 \right) \exp \left(-\frac{3}{4} \nu_A r_3^2 \right) d\vec{r}_1 d\vec{r}_2 d\vec{r}_3}_{\text{II}} \quad (45)$$

$$+ \underbrace{\frac{3}{4} \int r_3^2 \exp \left(-\frac{1}{2} \nu_A r_1^2 \right) \exp \left(-\frac{2}{3} \nu_A r_2^2 \right) \exp \left(-\frac{3}{4} \nu_A r_3^2 \right) d\vec{r}_1 d\vec{r}_2 d\vec{r}_3}_{\text{III}} \quad (46)$$

388 The first summand I can be calculated with $d\vec{r}_1 d\vec{r}_2 d\vec{r}_3 = (4\pi)^3 r_1^2 r_2^2 r_3^2 dr_1 dr_2 dr_3$ as

$$\text{I} = \frac{1}{2} (4\pi)^3 \cdot \int_0^\infty r_1^2 \exp \left(-\frac{1}{2} \nu_A r_1^2 \right) dr_1 \cdot \int_0^\infty \exp \left(-\frac{2}{3} \nu_A r_2^2 \right) dr_2 \cdot \int_0^\infty \exp \left(-\frac{3}{4} \nu_A r_3^2 \right) dr_3 \quad (47)$$

$$= \frac{1}{2} (4\pi)^3 \cdot \frac{3\sqrt{\pi}}{8} \frac{1}{(\frac{1}{2}\nu_A)^{5/2}} \cdot \frac{\sqrt{\pi}}{4} \frac{1}{(\frac{2}{3}\nu_A)^{3/2}} \cdot \frac{\sqrt{\pi}}{4} \frac{1}{(\frac{3}{4}\nu_A)^{3/2}}. \quad (48)$$

389 The other two summands II and III are evaluated accordingly and we thus obtain for the rms:

$$\lambda_4^2 = \frac{C_4^2}{4} (\text{I} + \text{II} + \text{III}) \quad (49)$$

$$= \frac{C_4^2}{4} (4\pi)^3 \frac{3\pi^{3/2}}{8 \cdot 4^2 \cdot \nu_A^{11/2}} \underbrace{\left(\frac{\frac{1}{2}}{(\frac{1}{2})^{5/2} (\frac{2}{3})^{3/2} (\frac{3}{4})^{3/2}} + \frac{\frac{2}{3}}{(\frac{1}{2})^{3/2} (\frac{2}{3})^{5/2} (\frac{3}{4})^{3/2}} + \frac{\frac{3}{4}}{(\frac{1}{2})^{3/2} (\frac{2}{3})^{3/2} (\frac{3}{4})^{5/2}} \right)}_{=24} \quad (50)$$

$$= \frac{9}{8\nu_A}. \quad (51)$$

C. HBT radii in Bertsch-Pratt and Yano-Koonin-Podgoretskii parameterisation for comparison with coalescence models

The results of HBT analyses are typically presented in either the Bertsch-Pratt (R_{out} , R_{side} , R_{long}) or the Yano-Koonin-Podgoretskii (R_{\perp} , R_0 , R_{\parallel}) parameterization. The ALICE HBT results [1, 43] are given in the Bertsch-Pratt convention, whereas the coalescence parameter is derived in [7] by expressing the dependence on the volume in terms of the Yano-Koonin-Podgoretskii (YKP) parameterisation. The transformation between the two parameterisations is best presented in [58] in the equations (W 3.48) to (W 3.52)²:

$$R_{side}^2 = R_{\perp}^2, \quad (52)$$

$$R_{diff}^2 = R_{out}^2 - R_{side}^2 = \beta_{\perp}^2 \gamma^2 (R_0^2 + v^2 R_{\parallel}^2), \quad (53)$$

$$R_{long}^2 = (1 - \beta_l^2) R_{\parallel}^2 + \gamma^2 (\beta_l - v)^2 (R_0^2 + v^2 R_{\parallel}^2), \quad (54)$$

$$R_{ol}^2 = \beta_{\perp} (-\beta_l R_{\parallel}^2 + \gamma^2 (\beta_l - v) (R_0^2 + v^2 R_{\parallel}^2)). \quad (55)$$

We immediately identify that R_{\perp}^2 can be identified with R_{side}^2 . Following the reasoning and the nomenclature in [58] (W 3.52-3.53), the above equations can be inverted and R_{\parallel}^2 can be expressed as

$$R_{\parallel}^2 = B - v \cdot C, \quad (56)$$

$$= R_{long}^2 - 2 \frac{\beta_l}{\beta_{\perp}} R_{ol}^2 + \frac{\beta_l^2}{\beta_{\perp}^2} R_{diff}^2 - v \cdot \left(-\frac{1}{\beta_{\perp}} R_{ol}^2 + \frac{\beta_l}{\beta_{\perp}^2} R_{diff}^2 \right). \quad (57)$$

As it turns out all corrections which are subtracted from R_{long}^2 can be neglected. First, we notice that the cross term R_{ol} vanishes if the measured fireball is longitudinally boost-invariant, which is a valid approximation for the rapidity ranges studied here. The remaining terms are all proportional to β_l . By definition of the rest frame for a longitudinally-boosted invariant system, $\beta_l = 0$. In summary, we can consider $R_{\perp} = R_{side}$ and $R_{\parallel} = R_{long}$ for the present study.

References

- [1] **ALICE** Collaboration, J. Adam *et al.*, “Centrality dependence of pion freeze-out radii in Pb-Pb collisions at $\sqrt{s_{NN}} = 2.76$ TeV,” *Phys. Rev.* **C93** no. 2, (2016) 024905, [arXiv:1507.06842 \[nucl-ex\]](#).
- [2] H. Nemura, Y. Suzuki, Y. Fujiwara, and C. Nakamoto, “Study of light Lambda and Lambda-Lambda hypernuclei with the stochastic variational method and effective Lambda N potentials,” *Prog. Theor. Phys.* **103** (2000) 929–958, [arXiv:nucl-th/9912065 \[nucl-th\]](#).
- [3] S. T. Butler and C. A. Pearson, “Deuterons from High-Energy Proton Bombardment of Matter,” *Phys. Rev.* **129** (1963) 836–842.
- [4] J. I. Kapusta, “Mechanisms for deuteron production in relativistic nuclear collisions,” *Phys. Rev.* **C21** (1980) 1301–1310.
- [5] H. Sato and K. Yazaki, “On the coalescence model for high-energy nuclear reactions,” *Phys. Lett.* **B98** (1981) 153–157.

²The equations in [58] are denoted as (W...) in order to distinguish them from the equations presented in this paper.

- [6] J. L. Nagle, B. S. Kumar, D. Kusnezov, H. Sorge, and R. Mattiello, “Coalescence of deuterons in relativistic heavy ion collisions,” *Phys. Rev.* **C53** (1996) 367–376.
- [7] R. Scheibl and U. W. Heinz, “Coalescence and flow in ultrarelativistic heavy ion collisions,” *Phys. Rev.* **C59** (1999) 1585–1602, [arXiv:nuc1-th/9809092](#) [nuc1-th].
- [8] **ExHIC** Collaboration, S. Cho *et al.*, “Exotic Hadrons from Heavy Ion Collisions,” *Prog. Part. Nucl. Phys.* **95** (2017) 279–322, [arXiv:1702.00486](#) [nuc1-th].
- [9] K. Blum, K. C. Y. Ng, R. Sato, and M. Takimoto, “Cosmic rays, antihelium, and an old navy spotlight,” *Phys. Rev.* **D96** no. 10, (2017) 103021, [arXiv:1704.05431](#) [astro-ph.HE].
- [10] S. Bazak and S. Mrowczynski, “ ${}^4\text{He}$ vs. ${}^4\text{Li}$ and production of light nuclei in relativistic heavy-ion collisions,” [arXiv:1802.08212](#) [nuc1-th].
- [11] W. Zhao, L. Zhu, H. Zheng, C. M. Ko, and H. Song, “Spectra and flow of light nuclei in relativistic heavy ion collisions at RHIC and the LHC,” [arXiv:1807.02813](#) [nuc1-th].
- [12] A. Andronic, P. Braun-Munzinger, K. Redlich, and J. Stachel, “Decoding the phase structure of QCD via particle production at high energy,” [arXiv:1710.09425](#) [nuc1-th].
- [13] A. Andronic, P. Braun-Munzinger, J. Stachel, and H. Stocker, “Production of light nuclei, hypernuclei and their antiparticles in relativistic nuclear collisions,” *Physics Letters B* **697** no. 3, (2011) 203 – 207.
- [14] **HotQCD** Collaboration, A. Bazavov *et al.*, “Equation of state in (2+1)-flavor QCD,” *Phys. Rev.* **D90** (2014) 094503, [arXiv:1407.6387](#) [hep-lat].
- [15] R. Bellwied, S. Borsanyi, Z. Fodor, S. D. Katz, and C. Ratti, “Is there a flavor hierarchy in the deconfinement transition of QCD?,” *Phys. Rev. Lett.* **111** (2013) 202302, [arXiv:1305.6297](#) [hep-lat].
- [16] **ALICE** Collaboration, B. Abelev *et al.*, “Centrality dependence of π , K, p production in Pb-Pb collisions at $\sqrt{s_{NN}} = 2.76$ TeV,” *Phys. Rev.* **C88** (2013) 044910, [arXiv:1303.0737](#) [hep-ex].
- [17] H. Garcilazo, “Pion deuteron break up in the region of the (3,3) resonance,” *Phys. Rev. Lett.* **48** (1982) 577–580.
- [18] S. A. Bass *et al.*, “Microscopic models for ultra-relativistic heavy ion collisions,” *Prog. Part. Nucl. Phys.* **41** (1998) 255–369, [arXiv:nuc1-th/9803035](#) [nuc1-th].
- [19] J. Schukraft, “QM2017: Status and Key open Questions in Ultra-Relativistic Heavy-Ion Physics,” *Nucl. Phys.* **A967** (2017) 1–10, [arXiv:1705.02646](#) [hep-ex].
- [20] **ALICE** Collaboration, S. Acharya *et al.*, “Measurement of deuteron spectra and elliptic flow in Pb-Pb collisions at $\sqrt{s_{NN}} = 2.76$ TeV at the LHC,” *Eur. Phys. J.* **C77** no. 10, (2017) 658, [arXiv:1707.07304](#) [nuc1-ex].
- [21] U. Heinz, “Coalescence model involving HBT and flow.” Presentation at EMMI Workshop in Torino, November 2017.
- [22] **ALICE** Collaboration, B. B. Abelev *et al.*, “ $K^*(892)^0$ and $\phi(1020)$ production in Pb-Pb collisions at $\sqrt{s_{NN}} = 2.76$ TeV,” *Phys. Rev.* **C91** (2015) 024609, [arXiv:1404.0495](#) [nuc1-ex].

- [23] C. Van Der Leun and C. Alderliesten, “The deuteron binding energy,” *Nucl. Phys.* **A380** (1982) 261–269.
- [24] P. J. Mohr, D. B. Newell, and B. N. Taylor, “CODATA Recommended Values of the Fundamental Physical Constants: 2014,” *Rev. Mod. Phys.* **88** no. 3, (2016) 035009, [arXiv:1507.07956 \[physics.atom-ph\]](#).
- [25] J. E. Purcell and C. G. Sheu, “Nuclear Data Sheets for $A = 3$,” *Nucl. Data Sheets* **130** (2015) 1–20.
- [26] D. H. Davis, “50 years of hypernuclear physics. I. The early experiments,” *Nucl. Phys.* **A754** (2005) 3–13.
- [27] M. Wang, G. Audi, F. Kondev, W. Huang, S. Naimi, and X. Xu, “The AME2016 atomic mass evaluation (II). Tables, graphs and references,” *Chinese Physics C* **41** no. 3, (2017) 030003.
- [28] I. Angeli and K. P. Marinova, “Table of experimental nuclear ground state charge radii: An update,” *Atom. Data Nucl. Data Tabl.* **99** no. 1, (2013) 69–95.
- [29] **A1** Collaboration, J. C. Bernauer *et al.*, “High-precision determination of the electric and magnetic form factors of the proton,” *Phys. Rev. Lett.* **105** (Dec, 2010) 242001.
- [30] S. Mrowczynski, “Production of light nuclei in the thermal and coalescence models,” *Acta Phys. Polon.* **B48** (2017) 707, [arXiv:1607.02267 \[nucl-th\]](#).
- [31] **AMS** Collaboration, J. Alcaraz *et al.*, “Search for anti-helium in cosmic rays,” *Phys. Lett.* **B461** (1999) 387–396, [arXiv:hep-ex/0002048 \[hep-ex\]](#).
- [32] S. Schael, “AMS-100 - A Magnetic Spectrometer at Lagrange Point 2.” Presentation at AMS days La Palma, April 2018.
- [33] **GAPS** Collaboration, T. Aramaki, C. J. Hailey, S. E. Boggs, P. von Doetinchem, H. Fuke, S. I. Mognet, R. A. Ong, K. Perez, and J. Zweerink, “Antideuteron Sensitivity for the GAPS Experiment,” *Astropart. Phys.* **74** (2016) 6–13, [arXiv:1506.02513 \[astro-ph.HE\]](#).
- [34] A. Esposito, A. L. Guerrieri, L. Maiani, F. Piccinini, A. Pilloni, A. D. Polosa, and V. Riquer, “Observation of light nuclei at ALICE and the X(3872) conundrum,” *Phys. Rev.* **D92** no. 3, (2015) 034028, [arXiv:1508.00295 \[hep-ph\]](#).
- [35] **ALICE** Collaboration, E. Abbas *et al.*, “Mid-rapidity anti-baryon to baryon ratios in pp collisions at $\sqrt{s} = 0.9, 2.76$ and 7 TeV measured by ALICE,” *Eur. Phys. J.* **C73** (2013) 2496, [arXiv:1305.1562 \[nucl-ex\]](#).
- [36] **ALICE** Collaboration, S. Acharya *et al.*, “Production of deuterons, tritons, ^3He nuclei and their anti-nuclei in pp collisions at $\sqrt{s} = 0.9, 2.76$ and 7 TeV,” *Phys. Rev.* **C97** no. 2, (2018) 024615, [arXiv:1709.08522 \[nucl-ex\]](#).
- [37] Anielski, Jonas, “Multiplicity Dependence of (Anti-)Deuteron Production in p-Pb Collisions at $\sqrt{s_{NN}} = 5.02$ TeV Measured with ALICE,” *J. Phys. Conf. Ser.* **612** no. 1, (2015) 012014.
- [38] **ALICE** Collaboration, J. Adam *et al.*, “ $^3_\Lambda\text{H}$ and $^3_\Lambda\bar{\text{H}}$ production in Pb-Pb collisions at $\sqrt{s_{NN}} = 2.76$ TeV,” *Phys. Lett.* **B754** (2016) 360–372, [arXiv:1506.08453 \[nucl-ex\]](#).
- [39] **ALICE** Collaboration, J. Adam *et al.*, “Production of light nuclei and anti-nuclei in pp and Pb-Pb collisions at energies available at the CERN Large Hadron Collider,” *Phys. Rev.* **C93** no. 2, (2016) 024917, [arXiv:1506.08951 \[nucl-ex\]](#).

- [40] A. Shebeko, P. Papakonstantinou, and E. Mavrommatis, “The One-body and two-body density matrices of finite nuclei with an appropriate treatment of the center-of-mass motion,” *Eur. Phys. J.* **A27** (2006) 143–155, [arXiv:nuc1-th/0602056](#) [nuc1-th].
- [41] Z. Zhang and C. M. Ko, “Hypertriton production in relativistic heavy ion collisions,” *Phys. Lett.* **B780** (2018) 191–195.
- [42] **ALICE** Collaboration, B. Abelev *et al.*, “Centrality determination of Pb-Pb collisions at $\sqrt{s_{NN}} = 2.76$ TeV with ALICE,” *Phys. Rev.* **C88** no. 4, (2013) 044909, [arXiv:1301.4361](#) [nuc1-ex].
- [43] **ALICE** Collaboration, K. Aamodt *et al.*, “Two-pion Bose-Einstein correlations in central Pb-Pb collisions at $\sqrt{s_{NN}} = 2.76$ TeV,” *Phys. Lett.* **B696** (2011) 328–337, [arXiv:1012.4035](#) [nuc1-ex].
- [44] **ALICE** Collaboration, J. Adam *et al.*, “Two-pion femtoscopy in p-Pb collisions at $\sqrt{s_{NN}} = 5.02$ TeV,” *Phys. Rev.* **C91** (2015) 034906, [arXiv:1502.00559](#) [nuc1-ex].
- [45] **ALICE** Collaboration, B. Abelev *et al.*, “Charged kaon femtosopic correlations in pp collisions at $\sqrt{s} = 7$ TeV,” *Phys. Rev.* **D87** no. 5, (2013) 052016, [arXiv:1212.5958](#) [hep-ex].
- [46] **ALICE** Collaboration, J. Adam *et al.*, “One-dimensional pion, kaon, and proton femtoscopy in Pb-Pb collisions at $\sqrt{s_{NN}} = 2.76$ TeV,” *Phys. Rev.* **C92** no. 5, (2015) 054908, [arXiv:1506.07884](#) [nuc1-ex].
- [47] M. Petran, J. Letessier, J. Rafelski, and G. Torrieri, “SHARE with CHARM,” *Comput. Phys. Commun.* **185** (2014) 2056–2079, [arXiv:1310.5108](#) [hep-ph].
- [48] S. Wheaton and J. Cleymans, “THERMUS: A Thermal model package for ROOT,” *Comput. Phys. Commun.* **180** (2009) 84–106, [arXiv:hep-ph/0407174](#) [hep-ph].
- [49] A. Andronic, P. Braun-Munzinger, and J. Stachel, “Hadron production in central nucleus-nucleus collisions at chemical freeze-out,” *Nucl. Phys.* **A772** (2006) 167–199, [arXiv:nuc1-th/0511071](#) [nuc1-th].
- [50] E. Schnedermann, J. Sollfrank, and U. W. Heinz, “Thermal phenomenology of hadrons from 200-A/GeV S+S collisions,” *Phys. Rev.* **C48** (1993) 2462–2475, [arXiv:nuc1-th/9307020](#) [nuc1-th].
- [51] **ALICE** Collaboration, B. Abelev *et al.*, “Pion, Kaon, and Proton Production in Central Pb–Pb Collisions at $\sqrt{s_{NN}} = 2.76$ TeV,” *Phys. Rev. Lett.* **109** (2012) 252301, [arXiv:1208.1974](#) [hep-ex].
- [52] **ALICE** Collaboration, B. B. Abelev *et al.*, “ K_S^0 and Λ production in Pb-Pb collisions at $\sqrt{s_{NN}} = 2.76$ TeV,” *Phys. Rev. Lett.* **111** (2013) 222301, [arXiv:1307.5530](#) [nuc1-ex].
- [53] V. Vovchenko and H. Stoecker, “Analysis of hadron yield data within hadron resonance gas model with multi-component eigenvolume corrections,” *J. Phys. Conf. Ser.* **779** no. 1, (2017) 012078, [arXiv:1610.02346](#) [nuc1-th].
- [54] **ALICE** Collaboration, J. Adam *et al.*, “Charged-particle multiplicities in proton?proton collisions at $\sqrt{s} = 0.9$ to 8 TeV,” *Eur. Phys. J.* **C77** no. 1, (2017) 33, [arXiv:1509.07541](#) [nuc1-ex].
- [55] T. Mart, L. Tiator, D. Drechsel, and C. Bennhold, “Electromagnetic production of the hypertriton,” *Nucl. Phys.* **A640** (1998) 235–258, [arXiv:nuc1-th/9610038](#) [nuc1-th].

- 544 [56] P. Artoisenet and E. Braaten, “Estimating the Production Rate of Loosely-bound
545 Hadronic Molecules using Event Generators,” *Phys. Rev.* **D83** (2011) 014019,
546 [arXiv:1007.2868 \[hep-ph\]](#).
- 547 [57] J. C. Bergstrom, “ ^6Li electromagnetic form factors and phenomenological cluster models,”
548 *Nucl. Phys.* **A327** (1979) 458–476.
- 549 [58] U. A. Wiedemann and U. W. Heinz, “Particle interferometry for relativistic heavy ion
550 collisions,” *Phys. Rept.* **319** (1999) 145–230, [arXiv:nucl-th/9901094 \[nucl-th\]](#).